A general model for welding of ash particles in volcanic systems validated using *in situ* x-ray tomography

Fabian B. Wadsworth[1,2,3], Jérémie Vasseur[3], Jenny Schauroth[4], Edward W. Llewellin[1], Katherine J. Dobson[1], Tegan Havard[1], Bettina Scheu[3], Felix W. von Aulock[4], James E. Gardner[5], Donald B. Dingwell[2,3], Kai-Uwe Hess[3], Mathieu Colombier[3], Federica Marone[6], Hugh Tuffen[7], Michael J. Heap[8]

[1]Department of Earth Sciences, Durham University, Durham, DH1 3LE, U.K. [2]Centre for Advanced Study, Ludwig-Maximilians-Universität, Munich, Germany. [3]Department of Earth and Environmental Science, Ludwig-Maximilians-Universität, Theresienstr. 41, Munich 80333, Germany. [4]School of Environmental Sciences, University of Liverpool, Jane Herdman Building, Liverpool L69 3GP, U.K. [5]Department of Geological Sciences, Jackson School of Geosciences, 2305 Speedway Stop C1160, Austin, TX 78712-1692, U.S. [6]Swiss Light Source, Paul Scherrer Institut, 5232 Villigen PSI, Switzerland. [7]Lancaster Environment Centre, Lancaster University, LA1 4YQ, U.K. [8]Institut de Physique du Globe de Strasbourg (UMR 7516 CNRS), Université de Strasbourg, 5 rue René Descartes, F-67084, Strasbourg, France.

sintering; porosity; synchrotron; surface tension; tomography; tuffisite; jet engine; obsidian

corresponding author: fabian.b.wadsworth@durham.ac.uk

Abstract:

Welding occurs during transport and deposition of volcanic particles in diverse settings, including pyroclastic density currents, volcanic conduits, and jet engines. Welding rate influences hazard-relevant processes, and is sensitive to water concentration in the melt. We characterize welding of fragments of crystal-free, water-supersaturated rhyolitic glass at high temperature using *in-situ* synchrotron-source x-ray tomography. Continuous measurement of evolving porosity and pore-space geometry reveals that porosity decays to a percolation threshold of $1-3$ vol.%, at which bubbles become isolated and welding ceases. We develop a new mathematical model for this process that combines sintering and water diffusion, which fits experimental data without requiring empirically-adjusted parameters. A key advance is that the model is valid for systems in which welding is driven by confining pressure, surface tension, or a combination of the two. We use the model to constrain welding timescales in a wide range of volcanic settings. We find that volcanic systems span the regime divide between capillary welding in which surface tension is important, and pressure welding in which confining pressure is important. Our model predicts that welding timescales in nature span seconds to years and that this is dominantly dependent on the particle viscosity or the evolution of this viscosity during particle degassing. We provide user-friendly tools, written in Python™ and in Excel™, to solve for the evolution of porosity and dissolved water concentration during welding for user-defined initial conditions.

Key points:

(1) First *in situ* determination of the welding rates of hydrous magma.

(2) A new mathematical model that couples volatile mass transfer with welding kinetics.

(3) This work provides a model relevant for ignimbrite and tuffisite welding

1. Introduction

Magma fragments into particles during explosive volcanic activity. Subsequent welding of these particles can occur at the base of hot pyroclastic density currents (Walker 1983; Branney et al. 1992), at the walls of volcanic conduits (Gonnermann and Manga 2003; Rust et al. 2004; Gardner et al. 2017), in tuffisite veins (Tuffen et al. 2003; Kendrick et al. 2016; Gardner et al. 2018), in the hot zone of jet engines (Giehl et al. 2016), and when lightning strikes volcanic ash in the air or on the ground (Cimarelli et al. 2017; Mueller et al. 2018). Despite this wide range of welding scenarios, there has been little work on the physics of welding of volcanic droplets, beyond simple empirical, semi-empirical, or scaling approaches (Friedman et al. 1963; Riehle 1973; Sparks et al. 1999; Quane and Russell 2005a; Russell and Quane 2005; Vasseur et al. 2013; Wadsworth et al. 2014).

Welding involves a reduction of inter-particle pore space (Branney and Kokelaar 1992; Sparks et al. 1999; Quane and Russell 2005a; Vasseur et al. 2013). Porosity is therefore a convenient metric for tracking the degree of welding, and has been used to rank the 'grade' of a welded deposit (Quane and Russell 2005b; Wright and Cashman 2014). Theoretical models for the evolution of porosity as a function of time in a welding system have been proposed (Frenkel 1945; Mackenzie and Shuttleworth 1949) but they do not account for the complexities of welding in magmatic systems, which include non-isothermal behavior, disequilibrium of dissolved volatile species, and the effect of a confining pressure that pushes the particles together. Non-isothermal behavior is important because welding in nature may occur as the particles cool (e.g. at conduit margins, within ejected ballistic bombs, or in ignimbrites) or follow more complex heating and cooling pathways (e.g. in a jet engine). Disequilibrium of volatile species – particularly of water – is important because the solubility changes as the pressure and temperature environment of the particles changes, driving diffusion in or out of the particles during welding (Sparks et al. 1999; Gardner et al. 2018). In the case of water, this

has a strong impact on the viscosity of the particle (Hess and Dingwell 1996) affecting welding rate (Grunder et al. 2005; Gardner et al. 2018, 2019). Confining (or lithostatic) pressure resulting, for example, from the weight of aggrading particles at the base of a pyroclastic density current, is important because it provides a stress that pushes the droplets together, accelerating welding. Previous theoretical and quantitative models for welding have focused on cases where welding is driven by surface tension alone (Wadsworth et al. 2016) or, where pressure is considered, have relied on scaling arguments (Sparks et al. 1999) or purely empirical correlations (e.g. Riehle 1973).

We develop a general and versatile mathematical framework for welding that can be used to predict the textural evolution of a welding pack of particles in a wide range of natural settings. We perform and analyze experiments conducted under non-isothermal, disequilibrium conditions to validate the model.

2. A theoretical model for droplet welding dynamics

2.1 Viscous welding under arbitrary pressure

Previous work on non-volcanic welding (or 'sintering') of spherical particles has shown that in the viscous state (i.e. when particles are droplets), surface-tension-driven welding is well described by a 'vented bubble model', in which the inter-droplet porosity is abstracted as a system of spherical bubbles in liquid shells, which are 'vented' so that the gas can escape as the bubbles shrink (Mackenzie and Shuttleworth 1949; Wadsworth et al. 2016). The geometric assumptions of the vented bubble model are most valid for highly polydisperse particle distributions (Wadsworth et al. 2017b) of the sort typical in nature, and the approximation becomes increasingly accurate as welding progresses because, as the droplets coalesce, the microstructural geometry continuously diverges from 'droplet-like' towards 'bubble-like' – that is, there is a topological inversion of the pore space (Wadsworth et al. 2017a). We start

from the assumption that the vented bubble model also applies to initially-angular particles. The conceptual steps in the geometric abstraction from an ash pack to a system of vented bubbles are shown in Figure 1.

We extend the vented bubble model to include a confining pressure that acts alongside surface tension stress to drive welding, where we use the term *confining* pressure to refer to an isotropic pressure acting to push the particles together – equivalently, when viewing the particles as viscous droplets, an isotropic pressure in the continuous liquid phase of the coalescing droplets. In their supplementary material, Wadsworth et al. (2016) derive the vented bubble model from the model of Prousevitch et al. (1993) for bubble growth in magma by setting the bubble pressure inside the associated liquid shell to be equal to the gas pressure outside the shell at all times. Here, we relax that assumption, and instead set the pressure difference to a value ΔP. Neglecting inertia, the full equation for the inter-droplet porosity ϕ with time t is then

$$\frac{d\phi}{dt} = -\frac{3\Delta P}{4\mu}\phi - \frac{3\Gamma}{2\mu a_i}\left(\frac{\phi_i}{1-\phi_i}\right)^{1/3}\phi^{2/3}(1-\phi)^{1/3}, \qquad \text{Eq. 1}$$

where ΔP is the difference between the confining pressure on the liquid droplets P_l and the pressure of the interstitial gas P_g, such that $\Delta P = P_l - P_g$, μ is the particle viscosity, Γ is the interfacial tension between the particles and the gas, a_i is the initial size of the bubble, and ϕ_i is the initial porosity when welding starts. A derivation of Eq. 1 from the Rayleigh-Plesset equation is given in the Supplementary Information.

Eq. 1 can be cast in dimensionless form by normalizing time to a characteristic capillary timescale $\lambda = \mu a_i/\Gamma$, such that $\bar{t} = t/\lambda$, normalizing pressure to a capillary pressure scale $P_c =$

$2\Gamma/a_i$, such that $\bar{P} = \Delta P/P_c$, and normalizing porosity to its initial value, such that $\bar{\phi} = \phi/\phi_i$, yielding

$$\frac{d\bar{\phi}}{d\bar{t}} = -\frac{3}{2}\left[\bar{P}\bar{\phi} + \left(\frac{1-\phi_i\bar{\phi}}{1-\phi_i}\right)^{1/3}\bar{\phi}^{2/3}\right], \quad \text{Eq. 2}$$

where a bar above a parameter denotes that it has been rendered dimensionless. The first term within the square brackets represents the contribution of the confining pressure, the second term represents the contribution of the capillary (Laplace) pressure.

The dimensionless time $\bar{t}$ can be generalized to account for non-isothermal temperature–time history, which is especially useful for natural magmatic scenarios. This is achieved by accounting for the change in viscosity μ as temperature varies, via

$$\bar{t} = \frac{t}{\lambda} = \frac{\Gamma}{a_i}\int_{t_\mathrm{i}}^{t}\frac{1}{\mu}dt \quad \text{Eq. 3}$$

where t_i is the time at which the welding process starts. In casting Eq. 3 this way, we assume that Γ is a constant, independent of time during welding. In reality, Γ is dependent on both water concentration and temperature, however, variations in surface tension are negligible compared with variations in liquid viscosity arising from the effects of both temperature and water concentration (discussed later). Together, Eqs 2 & 3 represent a universal description of isotropic, viscous particle welding, derived from micromechanical first principles. In the case where $\bar{P} = 0$, this approach has been validated against experimental data across a large range of temperatures (Wadsworth et al. 2016). While other models exist, they are either less easy to use, requiring a switch-point between two competing processes (Prado et al. 2001), or they rely

on bulk properties of the system, which have to be empirically determined and are therefore less general as they are not constructed from the micromechanics involved (Olevsky 1998; Quane and Russell 2005a).

The parameter a_i can be difficult to measure, or even define, for what is a complex, interconnected pore network (Figure 1). We use a relationship between a_i and the distribution of particle sizes $F(R)$ in a pack of particles or droplets (Lu and Torquato 1992), which is described in detail elsewhere (Wadsworth et al. 2016, 2017b). The relationship relies on knowledge of ϕ_i, and the moments of the distribution of R, denoted $\langle R^n \rangle$, which can be grouped into a polydispersivity factor $S = \langle R \rangle \langle R^2 \rangle / \langle R^3 \rangle$. The output from this is a pore size distribution $f(a_i)$ that relates to the particle size distribution $F(R)$ and ϕ_i, and is described in the Supplementary Information along with an account of how this is used in conjunction with Eqs 1-2 using convolution techniques (Wadsworth et al. 2017b).

2.2 Accounting for diffusion of volatiles during welding

In the model formulation above, the viscosity μ is assumed to be dependent on temperature, T, only. However, viscosity also depends on the concentration of water dissolved in the melt, which, in nature, may vary during welding. Volcanic particles formed at fragmentation may be super-saturated in dissolved water (Giachetti and Gonnermann 2013), and that super-saturation can grow as the particles ascend rapidly to lower pressures up-conduit without time to fully re-equilibrate (Gardner et al. 2017). Similarly, the solubility of water increases as the particles cool, which may cause them to re-hydrate (McIntosh et al. 2014; Ryan et al. 2015). Mass diffusion of water in or out of particles may occur on timescales similar to the timescale of welding (Sparks et al. 1999; Gardner et al. 2017, 2018, 2019); consequently, we anticipate that diffusion of water can affect the rate of welding through its impact on melt viscosity.

In order to account for diffusion, we must define the geometry of the internal welding system. The internal geometry of welding systems is complex and evolves from an initial state of particles in a gas continuum, to bubbles isolated in a liquid continuum. A rigorous solution for mass diffusion through this evolving geometry would require an approach that explicitly resolves both the fluid motion and the diffusion. However, as for the welding model, we simplify the problem by abstracting the geometry. For the purposes of diffusion modeling we assume that the particles remain spherical and simply apply Fick's 2nd law in spherical coordinates,

$$\frac{\partial C}{\partial t} = \frac{1}{r^2}\frac{\partial}{\partial r}\left(r^2 D \frac{\partial C}{\partial r}\right), \qquad \text{Eq. 4}$$

where C is the concentration of water in the melt particle, D is its diffusivity (which depends on temperature and local water concentration), and r is the radial position from the particle center. We adopt the assumption that the initial concentration of dissolved water C_i is uniform throughout the particle at the onset of welding, giving the initial condition $C = C_i$ for all r at $t = 0$. At all later times the water concentration at the surface of the particle is given by the equilibrium solubility C_e at the current conditions of gas pressure P_g and temperature T, giving the boundary condition $C = C_e(t)$ at $r = R$ for $t > 0$. We define a zero-flux boundary condition at the center of the particle: $\partial C/\partial r = 0$ at $r = 0$.

To account for the effect of variable water concentration in the particle we determine a spatial average by integrating C over $0 < r < R$; this integral is $\langle C \rangle = \int_0^1 C \, d\bar{r}$, where $\bar{r} = r/R$. We then use $\langle C \rangle$ to compute an average viscosity $\langle \mu \rangle$ which is used in Eqs 1-3 in place of μ. This approach results in an effective coupling between the diffusion model (Eq. 4) and the welding model (Eqs 1-3). In the Supplementary Information, we describe the numerical

solution of these equations in detail. We note here that our assumption of spherical particles undergoing diffusion of volatiles may be invalid at large polydispersivity for cases where the smallest particles are in equilibrium while the largest particles are far from equilibrium. This is discussed elsewhere (Gardner et al. 2019).

3. Experimental validation: materials and methods

Our starting material is a metaluminous, tholeiitic natural rhyolitic glass collected from Hrafntinnuhryggur, Krafla (Iceland). We crushed the obsidian to a powder using an agate mortar and pestle and then crushed the resultant chips to a fine powder using a concussion ball mill for short durations to prevent the sample heating significantly. The powder was sieved to < 125 μm diameter pieces and the size distribution was measured using a Beckman Coulter LS™ 230 laser refraction particle size analyzer with the measuring range $0.375 - 1000$ μm diameter. The particle size distribution is given in the Supplementary Information, and has a mean radius $\langle R \rangle = 2.2 \times 10^{-5}$ m.

Using a Netzsch Pegasus 404c device for simultaneous thermal analysis, we determined the dissolved volatile concentration that is excess (above solubility) at up to 1325 K to be $C_i = 0.15 \pm 0.02$ wt.%, by the relative loss of mass during heating, consistent with Tuffen and Castro (2009). This determination was performed on single chips ($n = 6$) from within a few millimeters of the sub-sample of the glass block that was used throughout this study.

To solve the governing equations given in our model, we require a parameterization for D, μ, and C_e relevant to the material in question. We use models relevant to the metaluminous rhyolites (Hess and Dingwell 1996; Liu et al. 2005; Zhang and Ni 2010)

$$\log_{10}(\mu) = -3.545 + 0.833 \ln(C) + \frac{9601 - 2368 \ln(C)}{T - 195.7 - 32.25 \ln(C)}$$

$$D = C \exp\left[-18.1 + 0.001888P_l - \left(\frac{9699 + 3.626P_l}{T}\right)\right]$$

$$C_e = \frac{354.941P_w^{0.5} + 9.623P_w - 1.5223P_w^{1.5}}{T} + 0.0012439P_w^{1.5} \quad \text{Eq. 5}$$

where P_w is the partial pressure of water in the interstitial gas phase, and the coefficients given are valid when T is in K, P_l and P_w are in MPa, and C and C_e are in wt.%. In the Supplementary Information we independently verify $\mu(T)$ for our material using a parallel plate compression method (Hess et al. 2007), a calorimetric method using a shift factor of 10.4 (Gottsmann et al. 2002), and a micropenetration method (Hess et al. 1995), which all demonstrate internal consistency, as well as matching the prediction of Eq. 5 for the measured C_i. We take a value $P_w = P_l\alpha$ with $\alpha = 0.2$, representing the typical humidity pressure in a laboratory furnace. Finally, we use $\Gamma = 0.3$ N.m^{-1}.

We performed two sets of *in situ* high temperature experiments, which used different methods to image the evolution of a welding pack of obsidian powder, lightly pressed into a free-standing cylinder with 3 mm diameter: (1) synchrotron-source x-ray tomography, providing continuous 3-dimensional microstructural data; and (2) optical dilatometry, providing bulk sample volume changes only. The first set of experiments were performed at the TOMCAT beamline of the Swiss Light Source at the Paul Scherer Institute. Cylinders of obsidian powder were loaded into the imaging window of the x-ray beam path. We used a laser system (Fife et al. 2012) to heat an alumina sleeve (muffle) placed over the samples, thus heating the obsidian pack indirectly. The temperatures measured by a pyrometer were calibrated by comparing the *in situ* welding of a well-studied sample of monodisperse glass beads with *ex situ* characterization of the same process (Wadsworth et al. 2016), resulting in a continuous correction for T, and confirming that temperature gradients on the sample scale were negligible. Full 3-dimensional tomographs were collected at 5.5×10^{-3} Hz with a spatial

resolution of 1.6 μm. The second set of experiments were performed using a Hesse Instruments EM-201 optical dilatometer, which continuously records the silhouette of the sample during heating at 1 Hz. Volume is determined from the silhouette as the solid of revolution.

The experiments covered a wide range of conditions, including isothermal experiments at temperatures of $1050 - 1500$ K, and linear heating ramps at rates of $0.04 - 0.25$ K. s^{-1}.The data from optical dilatometry are confined to porosity $\phi(t)$, while the tomography provides 3-dimensional data that are used to measure both the total porosity $\phi(t)$, and the porosity that is connected across the sample (or segmented domain) $\phi_p(t)$. After the heating experiments, we repeated the thermal analysis step on a few sub-samples, and no mass loss was observed, demonstrating the samples did equilibrate volatiles during the *in situ* experiments.

Supplementing our datasets collected at relatively low C_i and a small difference between C_i and C_e (small initial supersaturation), we re-analyse the data from Gardner et al. (2018) and Gardner et al. (2019). These data were collected at high P_g such that the equilibrium water concentration is also high. These data also include particles that hydrate and particles that de-hydrate while also welding.

All of the above experiments were conducted without confining pressure, hence $\bar{P} \approx 0$, a situation typical of small-scale laboratory settings. In order to examine the effect of $\bar{P} > 0$, we use data for welding Pyrex™ glass presented previously (Friedman et al. 1963). In those experiments the glass was crushed to a particle size around $100 - 250$ μm (not specified exactly), and welded under a uniaxial liquid pressure of $P_l = 1.52 \times 10^6$ Pa and $P_l = 3.63 \times 10^6$ Pa at temperatures $883 - 943$ K. We re-analyze these data using our model. While the same authors provide data for rhyolite particle welding (Friedman et al. 1963), some doubt exists as to the exact pressures used (Sparks et al. 1999) so we choose not to reanalyze those data.

4. Results, data analysis and model validation

In situ tomography allows us to render the evolving internal pore space of the samples in 3-dimensions through the welding process. Figure 2 shows a typical experimental result. The pore space is initially fully interconnected, and has a complex geometry between the angular glass fragments. As we heat the sample, the glass particles relax to liquid droplets at high temperature, and the droplet–droplet contacts weld. The porosity decreases with time smoothly and monotonically, and the rate at which it decreases depends strongly on temperature (in the isothermal experiments) or heating rate (in the non-isothermal experiments). The connectivity of the pore space drops during welding from fully connected at the start ($\phi_p/\phi = 1$), to fully closed at volume equilibrium ($\phi_p/\phi = 0$). The porosity at which the connectivity drops to zero is the percolation threshold porosity ϕ_c below which the system is impermeable. We determine this from our experiments as $\phi_c = 0.02 \pm 0.019$, which agrees with theory, simulations (Elam et al. 1984; Vasseur and Wadsworth 2017), and experiments (Wadsworth et al. 2016) in other welding droplet or overlapping sphere systems. This value is far lower than the percolation threshold for bubbly systems, as has previously been noted for the internal geometry of welding systems (Vasseur and Wadsworth 2017).

In Figures 2g & 3, we compare the results for the *in situ* x-ray tomography and optical dilatometry experiments with the model presented in section 2. For these unconfined laboratory-scale tests, the value of $\bar{P}$ is effectively 0. For the isothermal experiments we solve Eq. 2 with $\bar{P} = 0$, accounting for the diffusion of water out of the particles during welding via Eqs 3 & 4 (Figures 3a & 3b). For the non-isothermal experiments we additionally account for temperature change via Eq. 3 (Figure 3c). In both cases, we find good agreement and a reasonable collapse of the data to the model. This result highlights that, in these experiments, welding rates are influenced by temperature and volatile content, both of which control the

277 particle viscosity and can evolve on the same timescale as the welding; hence, they must be
278 solved explicitly (Eqs 3 & 4). Welding rate also depends on particle size distribution, interfacial
279 tension, and the initial porosity of the packed particles. Particle angularity may subtly affect
280 both the diffusion rate and the sintering rate when compared with the model, which is based on
281 idealised spherical particles, but, given the good agreement between model and data, this effect
282 does not appear to be of first-order.

283 The experimental validation of our simple model for $\bar{P} = 0$ appears to be successful. To
284 extend this to conditions where $\bar{P} > 0$, we re-analyse the results from Friedman et al. (1963)
285 in which anhydrous glass was heated under pressure. In the Supplementary Information we
286 give a detailed description of the methods used in Friedman et al (1963), but note here that Eqs
287 1 and 2 are valid in their experiments. We assume that the uniaxial nature of their applied loads
288 can be accounted for using the Trouton ratio, such that our model for isotropic pressurization
289 can be adapted to uniaxial conditions. For their anhydrous experiments, conducted at $\bar{P} = 100$,
290 we apply Eq. 2 directly. We find good agreement across a wide range of temperature (Figure
291 4), validating our model up to naturally relevant pressures and across the regime boundary $\bar{P} =$
292 1. These conditions represent the state where the volcanic particles are under pressure, but the
293 interconnected gas phase between the particles remain un-pressurized, which is a typical
294 scenario for larger systems in nature. We show that, in this case, the time required for welding
295 to complete is reduced by the elevated confining pressure, as implied by Eq. 2 (note how the
296 data collapse to a model curve to the left of the $\bar{P} = 0$ curve in Figure 4, and are therefore
297 welding more rapidly).

298

299 **5. Discussion**

300 **5.1 Validity of the welding model**

The welding model agrees well with experimental data across a wide range of conditions, validating the model for application to welding systems: 1) with and without applied pressure; 2) under isothermal and non-isothermal conditions; 3) in which dissolved water is in equilibrium or disequilibrium with ambient pressure and temperature conditions. Thus the model is sufficiently general to capture most of the essential features of welding scenarios in magmatic and volcanic systems. There are, however, two limitations. Firstly, the model does not apply directly to welding under high shearing stress. We do use experimental data in which welding particles are under uniaxial compression (Friedman et al. 1963), such that the anisotropy of the pressure applied results in shear stresses internal to the sample (c.f. uniaxial experiments in Quane and Russell 2005; Heap et al. 2015), which we account for via the Trouton ratio. This gives us some confidence that, under minor local shearing within a system that is loaded anisotropically, our model is valid. Nonetheless, we note that validation for shearing systems requires future systematic study over a larger range of better constrained shear stress. This limitation means that our model does not, for example, explicitly predict the formation of fiammé in welded ignimbrites. Secondly, the model assumes that interstitial gas escapes freely from the welding system, and does not apply when gas escape is significantly hindered by the permeability of the connected pore network. We can determine the conditions under which this second limitation is important.

The characteristic lengthscale beyond which a viscous system is permeability-limited is the compaction length $L_c = \left(k_r \mu / \mu_g\right)^{1/2}$ (Michaut et al. 2009; Kennedy et al. 2016), where k_r is a reference permeability and μ_g is the gas viscosity. If we normalize our system length by L_c we have

$$\bar{L} = \frac{L}{L_c} \approx L\sqrt{\frac{\mu_g}{k_r \mu}}. \qquad \text{Eq. 6}$$

If $\bar{L} \gg 1$, permeability is a rate-limiting parameter, with the consequence that P_g may rise in parts of the system and affect the welding rate (because the welding rate depends is sensitive to $P_c - P_g$); this regime is termed *compaction welding*. If $\bar{L} \ll 1$, gas escape can occur more rapidly than welding occurs and the process is not hindered by sluggish gas escape. The analysis presented via Eqs 1-4 is therefore valid in the regime $\bar{L} \ll 1$.

5.2 Welding regimes in nature

The dimensionless length $\bar{L}$ discriminates between regimes in which welding is or is not limited by permeable outgassing of the interstitial gas phase. For the non-limited regime ($\bar{L} \ll 1$) in which our welding model is valid, we can also discriminate between regimes in which welding is dominated by confining pressure (*pressure welding*), or by capillary pressure arising from the surface tension (*capillary welding*). From Eq. 2, we see that the confining pressure term dominates the capillary pressure term when

$$\begin{aligned} \bar{P} &\gg \left(\frac{1-\phi_i\bar{\phi}}{\bar{\phi}-\bar{\phi}\phi_i}\right)^{1/3} \quad \text{pressure welding,} \\ \bar{P} &\ll \left(\frac{1-\phi_i\bar{\phi}}{\bar{\phi}-\bar{\phi}\phi_i}\right)^{1/3} \quad \text{capillary welding.} \end{aligned} \qquad \text{Eq. 7}$$

The dependence on the porosity (via $\bar{\phi}$) arises because capillary stress always tends towards infinity as bubble radius tends towards zero, such that a system that starts in the pressure welding regime may end in the capillary regime with no change in the ambient conditions. The value of the terms on the right hand side of Eq. 7 is equal to unity at the start of welding so, in

practice we use $\bar{P} \gg 1$ and $\bar{P} \ll 1$ to discriminate between pressure and capillary welding regimes.

Given these constraints ($\bar{P}$ and $\bar{L}$), we can assess the regimes covered by some typical volcanic welding scenarios. For any situation in which welding might occur, we therefore need to know μ, R_i, L, and ΔP (for simplicity, we take a constant $\Gamma = 0.3\ \mathrm{N.m^{-1}}$ (Wadsworth et al. 2016), $\mu_g \approx 10^{-5}$ Pa.s, and $k_r = k_i \approx 7 \times 10^{-12}\ \mathrm{m^2}$ for packed particles (Wadsworth et al. 2017a)). For these dimensional considerations we assume that $a_i = R_i$, because there is usually insufficient information provided to compute a_i explicitly, and we justify this by noting that these values are typically of the same order of magnitude (Wadsworth et al. 2016). In Table 1 we give a compilation of estimated values for these parameters gathered from well-studied welded ignimbrites, tuffisites, welded jet engine deposits, and welded obsidian pyroclasts. In each case, these parameters are converted to a quantitative range of $\bar{P}$ and $\bar{L}$ that represents the initial conditions for that particular system, and plotted in Figure 5. In the case of tuffisites from Volcán Colima, we use the values of particle (droplet) viscosity from Kendrick et al. (2016) which incorporate the effect of crystallinity.

We find that very few systems are in the $\bar{L} \gg 1$ (permeability limited) regime. Exceptions would include welding in particularly large welded ignimbrite systems if the emplacement mode is *en masse* (we give the result for the $L \leq 400$ m Bad Step Tuff, for which $\bar{L}$ can exceed unity). However, under the assumption of the progressive-aggradation model for the sedimentation of ignimbrites (Branney and Kokelaar 1992) and an estimated, rising $L \approx 2$ m thick welding window (Andrews and Branney 2011), we find that $\bar{L} \ll 1$ is more typical for ignimbrite emplacement. The *en masse* and progressive aggradation models for ignimbrite emplacement represent upper and lower bounds on $\bar{L}$, respectively.

We also find that volcanic welding scenarios span the $\bar{P} = 1$ divide, implying that there are cases for which pressure welding dominates ($\bar{P} > 1$) and cases for which capillary welding

dominates ($0 \leq |\bar{P}| < 1$). Pressure welding appears to be typical of tuffisites and ignimbrites, while capillary welding appears to be typical of the formation of obsidian pyroclasts and of undesirable welding in the combustion chamber of jet engines (Figure 5). Tuffisites, in particular, are known to have variable and complex pressure–temperature histories, implying that they may track through $\bar{P}$ space during their formation and welding (Tuffen and Dingwell 2005; Castro et al. 2012; Saubin et al. 2016). If the exact evolution of pressure and temperature were known, then our model could be used to determine the degree of welding throughout.

For each of the cases presented in Figure 5, we can compute a timescale for the porosity to reach the equilibrium value $\phi = \phi_c$. For systems welding at any $\bar{P}$, for $\bar{L} \ll 1$, this timescale includes contributions from the pressure and capillary components, and can be taken as the reciprocal of the sum of the characteristic welding rates associated with the confining pressure and capillary pressure terms

$$\lambda_W \approx \left(\frac{\Delta P}{\langle \mu \rangle} + \frac{\Gamma}{\langle \mu \rangle \langle R_i \rangle}\right)^{-1}. \qquad \text{Eq. 8}$$

We use Eq. 8 and the inputs in Table 1 to compute λ_W (in seconds) for each case study example given. We find that most systems weld over a timescale of 1 second to 1 day. Exceptions, which require very long timescales to weld, are crystal-rich tuffisites (Kendrick et al. 2016) or obsidian pyroclasts welding under the lowest temperature and gas pressure conditions expected (Gardner et al. 2017). In both of those slow-welding scenarios, it is unlikely that welding will complete before other processes, such as cooling of the particles or deposit, terminate welding. However, remarkably, the welding timescale for most rhyolitic systems investigated appears to span a similar range regardless of the $\bar{P}$ of formation; hence $\langle \mu \rangle$, and therefore the degassing

391 and temperature history, is the most important controlling parameter in welding for rhyolitic
392 magmas.
393
394 **5.3 User-friendly computational tools for solving welding problems in volcanic scenarios in**
395 **Python™ and Excel™**
396 As part of this contribution, we provide a downloadable executable file for Linux™ and Mac
397 platforms, which solves the full diffusion–welding problem given here. The executable
398 requires the following user inputs: particle size distribution (as a .txt or .csv file), initial
399 porosity ϕ_i, initial dissolved water concentration C_i, initial temperature, gas pressure P_g,
400 pressure differential $\Delta P = P_l - P_g$, surface tension Γ, and the spatial resolution for the
401 diffusion solution (we set a default value of 100 steps, which is sufficient for most cases). We
402 additionally allow the user to input a temperature rate, which should be positive for heating,
403 negative for cooling, or zero for isothermal conditions, and which imposes a linear change in
404 temperature. The outputs of this code are the monodisperse or polydisperse solutions for
405 porosity as a function of time and the value of $\langle C \rangle$. Similarly, we provide an editable Excel™
406 sheet for solving our welding code for isothermal or non-isothermal conditions including for
407 polydisperse particles (or droplets), but without diffusion of volatiles. This code is available
408 via VHub (https://vhub.org/resources/4568).
409
410
411 **6 Concluding remarks**
412 We present a universal theoretical model of welding of natural volcanic material at relevant
413 volcanic conditions. The model includes the complex effect of syn-welding dehydration,
414 accounts for the effects of confining pressure and capillary pressure, and is valid for both

415 isothermal and non-isothermal conditions. The welding model is grounded in the microphysical
416 behaviour of a welding system, and requires no fitting parameters.

417 We use scaling arguments to assess the validity of the model for natural welding
418 scenarios, and conclude that it can be applied to welding in tuffisites, in volcanic conduits, at
419 the base of aggrading pyroclastic density currents, and in jet engines. Our model predicts that
420 volcanic systems span the divide between the regime in which the capillary stress at particle
421 walls drives welding, and the regime in which the driving pressure for welding is the difference
422 between the liquid and the interstitial gas pressures. We find that in most cases examined here,
423 the permeability of the interstitial gas phase does not limit the welding dynamics. Finally, we
424 find that the total time required for complete welding spans seconds to years, and that the
425 viscosity of the particles, or the evolution of viscosity during particle degassing, is the most
426 variable parameter in nature.

427 The model we present provides a flexible and general tool for investigating welding
428 phenomena across a wide range of volcanically-relevant scenarios. The model solution is given
429 for the specific case of rhyolite welding via a vHub resource.

430

431

Acknowledgements

We acknowledge European Research Council Advanced Grant EVOKES 247076, UK NERC grants NE/N002954/1 and No. NE/M018687/1, a fellowship from the Institute of Advanced Study at Durham University (to J. Gardner) and from the Centre for Advanced Study at LMU, Munich (to F. Wadsworth), a Royal Society University Research Fellowship (to H. Tuffen) and Royal Society International Exchange grant (to H. Tuffen and M. Heap), and the VUELCO consortium funded under the EU's FP7 grant agreement 282759. The Paul-Scherer-Institute (Swiss Light Source) awarded beamtime under proposals No. 20141231 and No. 20150413 at the TOMCAT beamline. Thanks to Yan Lavallée and Jackie Kendrick for valuable discussions and for supporting J. Schauroth's contribution to this work. S. Wiesmaier is thanked for assistance on the beamline. All raw data are available on request from the authors. Codes available via VHub at https://vhub.org/resources/4568. We thank Tamsin Mather for editorial handling, and Stephan Kolzenburg and an anonymous reviewer for constructive comments.

Author contributions to this work

The team at the TOMCAT beamline (PSI, Switzerland) included F.B. Wadsworth (team lead), J. Vasseur, E.W. Llewellin, K.J. Dobson, F.W. von Aulock, J. Fife, and F. Marone. J. Schauroth and K.J. Dobson processed the 3D datasets and extracted raw data. F.B. Wadsworth, J. Vasseur, and E.W. Llewellin performed the analysis and model development. F.B. Wadsworth, J. Schauroth, J.E. Gardner, K.-U. Hess, M.J. Heap, H. Tuffen, and D.B. Dingwell provided additional *ex situ* or calibration data for analysis and consulted on the data treatment and the manuscript. F.B. Wadsworth, J. Schauroth, and E.W. Llewellin led the drafting of a manuscript text with help from all authors. T. Havard compiled data from natural deposits.

References cited

Andrews GDM, Branney MJ (2011) Emplacement and rheomorphic deformation of a large, lava-like rhyolitic ignimbrite: Grey's Landing, southern Idaho. Geol Soc Am Bull 123:725–743. doi: 10.1130/b30167.1

Branney M, Kokelaar Bp, McConnell B (1992) The Bad Step Tuff: a lava-like rheomorphic ignimbrite in a calc-alkaline piecemeal caldera, English Lake District. Bull Volcanol 54:187–199. doi: 10.1007/BF00278388

Branney M, Kokelaar P (1992) A reappraisal of ignimbrite emplacement: progressive aggradation and changes from particulate to non-particulate flow during emplacement of high-grade ignimbrite. Bull Volcanol 54:504–520. doi: 10.1007/BF00301396

Castro JM, Bindeman IN, Tuffen H, Ian Schipper C (2014) Explosive origin of silicic lava: Textural and δD-H2O evidence for pyroclastic degassing during rhyolite effusion. Earth Planet Sci Lett 405:52–61. doi: 10.1016/j.epsl.2014.08.012

Castro JM, Cordonnier B, Tuffen H, et al (2012) The role of melt-fracture degassing in defusing explosive rhyolite eruptions at volcán Chaitén. Earth Planet Sci Lett 333:63–69. doi: http://dx.doi.org/10.1016/j.epsl.2012.04.024

Cimarelli C, Yilmaz T, Colombier M, et al (2017) Micro-and nano-CT textural analysis of an experimental volcanic fulgurite. EGU Gen Assem Conf Abstr 19:17982

Clarke AB, Voight B (2000) Pyroclastic current dynamic pressure from aerodynamics of tree or pole blow-down. J Volcanol Geotherm Res 100:395–412. doi: 10.1016/S0377-0273(00)00148-7

Elam WT, Kerstein AR, Rehr JJ (1984) Critical properties of the void percolation problem for spheres. Phys Rev Lett 52:1516

Fife JL, Rappaz M, Pistone M, et al (2012) Development of a laser-based heating system for in situ synchrotron-based X-ray tomographic microscopy. J Synchrotron Radiat 19:352–

484 358
485 Frenkel J (1945) Viscous flow of crystalline bodies under the action of surface tension. J
486 Phys 9:385–391
487 Friedman I, Long W, Smith RL (1963) Viscosity and water content of rhyolite glass. J
488 Geophys Res 68:6523–6535
489 Gardner JE, Llewellin EW, Watkins JM, Befus KS (2017) Formation of obsidian pyroclasts
490 by sintering of ash particles in the volcanic conduit. Earth Planet Sci Lett 459:252–263.
491 doi: 10.1016/J.EPSL.2016.11.037
492 Gardner JE, Wadsworth FB, Llewellin EW, et al (2018) Experimental sintering of ash at
493 conduit conditions and implications for the longevity of tuffisites. Bull Volcanol 80:23.
494 doi: 10.1007/s00445-018-1202-8
495 Gardner JE, Wadsworth FB, Llewellin EW, et al (2019) Experimental constraints on the
496 textures and origin of obsidian pyroclasts. Bull Volcanol 81:22. doi: 10.1007/s00445-
497 019-1283-z
498 Giachetti T, Gonnermann HM (2013) Water in volcanic pyroclast: Rehydration or incomplete
499 degassing? Earth Planet Sci Lett 369–370:317–332. doi: 10.1016/J.EPSL.2013.03.041
500 Giehl C, Brooker R, Marxer H, Nowak M (2016) An experimental simulation of volcanic ash
501 deposition in gas turbines and implications for jet engine safety. Chem Geol
502 Giordano D, Russell JK, Dingwell DB (2008) Viscosity of magmatic liquids: a model. Earth
503 Planet Sci Lett 271:123–134
504 Gonnermann HM, Manga M (2003) Explosive volcanism may not be an inevitable
505 consequence of magma fragmentation. Nature 426:432–435
506 Gottsmann J, Giordano D, Dingwell DB (2002) Predicting shear viscosity during volcanic
507 processes at the glass transition: a calorimetric calibration. Earth Planet Sci Lett
508 198:417–427

509 Grunder AL, Laporte D, Druitt TH (2005) Experimental and textural investigation of
510 welding: effects of compaction, sintering, and vapor-phase crystallization in the rhyolitic
511 Rattlesnake Tuff. J Volcanol Geotherm Res 142:89–104. doi:
512 http://dx.doi.org/10.1016/j.jvolgeores.2004.10.018
513 Heap MJ, Farquharson JI, Wadsworth FB, et al (2015) Timescales for permeability reduction
514 and strength recovery in densifying magma. Earth Planet Sci Lett 429:223–233. doi:
515 10.1016/j.epsl.2015.07.053
516 Hess KU, Cordonnier B, Lavallee Y, Dingwell DB (2007) High-load, high-temperature
517 deformation apparatus for synthetic and natural silicate melts. Rev Sci Instrum
518 78:75102. doi: 10.1063/1.2751398
519 Hess KU, Dingwell DB (1996) Viscosities of hydrous leucogranitic melts: A non-Arrhenian
520 model. Am Mineral 81:1297–1300
521 Hess KU, Dingwell DB, Webb SL (1995) The influence of excess alkalis on the viscosity of
522 a haplogranitic melt. Am Mineral 80:297–304
523 Kendrick JE, Lavallée Y, Varley NR, et al (2016) Blowing off steam: Tuffisite formation as a
524 regulator for lava dome eruptions. Front Earth Sci 4:. doi: 10.3389/feart.2016.00041
525 Kennedy BM, Wadsworth FB, Vasseur J, et al (2016) Surface tension driven processes
526 densify and retain permeability in magma and lava. Earth Planet Sci Lett 433:116–124.
527 doi: 10.1016/j.epsl.2015.10.031
528 Liu Y, Zhang Y, Behrens H (2005) Solubility of H< sub> 2</sub> O in rhyolitic melts at low
529 pressures and a new empirical model for mixed H< sub> 2</sub> O–CO< sub> 2</sub>
530 solubility in rhyolitic melts. J Volcanol Geotherm Res 143:219–235
531 Lu B, Torquato S (1992) Nearest-surface distribution functions for polydispersed particle
532 systems. Phys Rev A 45:5530
533 Mackenzie JK, Shuttleworth R (1949) A phenomenological theory of sintering. Proc Phys

534 Soc Sect B 62:833
535 McIntosh IM, Llewellin EW, Humphreys MCS, et al (2014) Distribution of dissolved water
536 in magmatic glass records growth and resorption of bubbles. Earth Planet Sci Lett
537 401:1–11. doi: 10.1016/j.epsl.2014.05.037
538 Michaut C, Bercovici D, Sparks RSJ (2009) Ascent and compaction of gas rich magma and
539 the effects of hysteretic permeability. Earth Planet Sci Lett 282:258–267
540 Mueller SP, Helo C, Keller F, et al (2018) First experimental observations on melting and
541 chemical modification of volcanic ash during lightning interaction. Sci Rep 8:1389. doi:
542 10.1038/s41598-018-19608-3
543 Olevsky EA (1998) Theory of sintering: from discrete to continuum. Mater Sci Eng R
544 Reports 23:41–100
545 Prado M, Dutra Zanotto E, Müller R (2001) Model for sintering polydispersed glass particles.
546 J Non Cryst Solids 279:169–178
547 Prousevitch AA, Sahagian DL, Anderson AT (1993) Dynamics of diffusive bubble growth in
548 magmas: isothermal case. J Geophys Res Solid Earth 98:22283–22307. doi:
549 10.1029/93JB02027
550 Quane SL, Russell JK (2005a) Welding: insights from high-temperature analogue
551 experiments. J Volcanol Geotherm Res 142:67–87. doi:
552 http://dx.doi.org/10.1016/j.jvolgeores.2004.10.014
553 Quane SL, Russell JK (2005b) Ranking welding intensity in pyroclastic deposits. Bull
554 Volcanol 67:129–143
555 Riehle JR (1973) Calculated Compaction Profiles of Rhyolitic Ash-Flow Tuffs. Bull Geol
556 Soc Am 84:2193–2216. doi: 10.1130/0016-7606(1973)84<2193:CCPORA>2.0.CO;2
557 Russell JK, Quane SL (2005) Rheology of welding: inversion of field constraints. J Volcanol
558 Geotherm Res 142:173–191. doi: http://dx.doi.org/10.1016/j.jvolgeores.2004.10.017

559 Rust AC, Cashman K V, Wallace PJ (2004) Magma degassing buffered by vapor flow
560 through brecciated conduit margins. Geology 32:349–352
561 Ryan AG, Russell JK, Nichols ARL, et al (2015) Experiments and models on H2O retrograde
562 solubility in volcanic systems. Am Mineral 100:774–786. doi: 10.2138/am-2015-5030
563 Saubin E, Tuffen H, Gurioli L, et al (2016) Conduit Dynamics in Transitional Rhyolitic
564 Activity Recorded by Tuffisite Vein Textures from the 2008–2009 Chaitén Eruption.
565 Front Earth Sci 4:. doi: 10.3389/feart.2016.00059
566 Sparks RSJ, Tait SR, Yanev Y (1999) Dense welding caused by volatile resorption. J Geol
567 Soc London 156:217–225. doi: 10.1144/gsjgs.156.2.0217
568 Streck MJ, Grunder AL (1995) Crystallization and welding variations in a widespread
569 ignimbrite sheet; the Rattlesnake Tuff, eastern Oregon, USA. Bull Volcanol 57:151–169
570 Sumner JM, Branney MJ (2002) The emplacement history of a remarkable heterogeneous,
571 chemically zoned, rheomorphic and locally lava-like ignimbrite: 'TL' on Gran Canaria.
572 J Volcanol Geotherm Res 115:109–138. doi: 10.1016/S0377-0273(01)00311-0
573 Tuffen H, Castro JM (2009) The emplacement of an obsidian dyke through thin ice:
574 Hrafntinnuhryggur, Krafla Iceland. J Volcanol Geotherm Res 185:352–366
575 Tuffen H, Dingwell D (2005) Fault textures in volcanic conduits: evidence for seismic trigger
576 mechanisms during silicic eruptions. Bull Volcanol 67:370–387. doi: 10.1007/s00445-
577 004-0383-5
578 Tuffen H, Dingwell DB, Pinkerton H (2003) Repeated fracture and healing of silicic magma
579 generate flow banding and earthquakes? Geology 31:1089–1092. doi: 10.1130/g19777.1
580 Vasseur J, Wadsworth FB (2017) Sphere models for pore geometry and fluid permeability in
581 heterogeneous magmas. Bull Volcanol 79:. doi: 10.1007/s00445-017-1165-1
582 Vasseur J, Wadsworth FB, Lavallée Y, et al (2013) Volcanic sintering: Timescales of viscous
583 densification and strength recovery. Geophys Res Lett 40:5658–5664. doi:

584 10.1002/2013GL058105
585 Wadsworth FB, Vasseur J, Aulock FW, et al (2014) Nonisothermal viscous sintering of
586 volcanic ash. J Geophys Res Solid Earth 119:8792–8804
587 Wadsworth FB, Vasseur J, Llewellin EW, et al (2016) Sintering of viscous droplets under
588 surface tension. Proc R Soc A Math Phys Eng Sci 472:20150780. doi:
589 10.1098/rspa.2015.0780
590 Wadsworth FB, Vasseur J, Llewellin EW, et al (2017a) Topological inversions in coalescing
591 granular media control fluid-flow regimes. Phys Rev E 96:. doi:
592 10.1103/PhysRevE.96.033113
593 Wadsworth FB, Vasseur J, Llewellin EW, Dingwell DB (2017b) Sintering of polydisperse
594 viscous droplets. Phys Rev E 95:033114. doi: 10.1103/PhysRevE.95.033114
595 Walker GPL (1983) Ignimbrite types and ignimbrite problems. J Volcanol Geotherm Res
596 17:65–88. doi: 10.1016/0377-0273(83)90062-8
597 Wright HM, Cashman K V (2014) Compaction and gas loss in welded pyroclastic deposits as
598 revealed by porosity, permeability, and electrical conductivity measurements of the
599 Shevlin Park Tuff. Geol Soc Am Bull 126:234–247. doi: 10.1130/b30668.1
600 Zhang Y, Ni H (2010) Diffusion of H, C, and O components in silicate melts. Rev Mineral
601 Geochemistry 72:171–225
602

603

Table 1 Constraints underpinning $\bar{P}$ and $\bar{L}$ from natural deposits or scenarios

	Particle viscosity[#] μ (Pa.s)	System length L (m)	Particle radius[$] R_i (m)	Liquid pressure P_l (Pa)	Gas pressure P_g (Pa)	Initial water content[**] C_i (wt.%)	Emplacement temperature[**] T (K)	References
Welded ignimbrites								
Bad Step Tuff	10^7-10^8	40-400[*]	10^{-5}-10^{-3}	10^6-10^7	10^5-10^6	0.1-0.2	1273	(Branney et al. 1992)
TL	10^5-10^6	10.4-28[*]	10^{-5}-10^{-3}	3.1-7.5x10^5	10^5-10^6	0.47-0.87	1084-1183	(Sumner and Branney 2002)
Grey's Landing	10^7-10^9	2-70[*]	10^{-5}-10^{-3}	10^5-10^6	10^5-10^6	0.1-0.2	1198-1298	(Andrews and Branney 2011)
Rattlesnake tuff	10^8-10^{10}	15-70[*]	10^{-5}-10^{-3}	4.1x10^5-10^6	10^5-10^6	0.1-0.2	1073-1153	(Streck and Grunder 1995)
Tuffisites								
Chaitén (2008)	10^7-10^9	0.005-0.03	1.25x10^{-4}-2.5x10^{-4}	10^6-10^7	4.6x10^6-8.1x10^6	0.44-1.2	1023-1098	(Castro et al. 2012; Saubin et al. 2016)
Cordon Caulle 2011-2013	10^8-10^9	0.005-0.03	10^{-6}-10^{-3}	10^6-10^7	4.6x10^6-8.1x10^6	0.16-0.25	1168	(Castro et al. 2014)
Colima	10^{10}-10^{11}	0.001-0.05	10^{-4}-10^{-3}	10^5-10^6	10^5	0.1-0.2	1213-1253	(Kendrick et al. 2016)
Törfajökull	10^9-10^{14}	0.001-0.05	10^{-5}-10^{-3}	10^6-10^7	4.6x10^6-8.1x10^6			(Tuffen and Dingwell 2005)
Obsidian pyroclasts								
Mono craters	10^6-10^{12}	0.01-0.02	2x10^{-5}-1.7x10^{-4}	1.002x10^5	10^5			(Gardner et al. 2017)
Jet engine deposits								
Rhyolitic experimental	10^3-10^9	10^{-3}-10^{-2}	3x10^{-5}	4.0002x10^6	4x10^6	0.1	1148-1848	(Giehl et al. 2016)

[#]The viscosity is either taken from the references for each case study or otherwise is calculated using *Hess and Dingwell*, [1996] with the C_i and T given for most cases (exceptions are the TL ignimbrite and the basaltic example for the jet engine deposits, both of which are calculated using *Giordano et al.*, [2008] and the composition given in the references; for TL, we use the WTL trachyte zone composition because this is the 'lava like' facies (Sumner and Branney 2002)).

[*]This system length is assuming *en masse* deposition, but for progressive aggradation we take 2 m for all ignimbrites

[+]We take this liquid pressure to be the hydrostatic loading pressure assuming a density of 2300 kg.m^{-3}. Except for the tuffisite cases, the gas pressure is added to the liquid pressure.

[£]The upper limit of these gas pressures is given by estimates of dynamic pressures during transport in pyroclastic density currents (Clarke and Voight 2000).

[**]Note that these parameters are only required if the viscosity is not given directly by the originating authors. The value for C_i is approximated as 0.1-0.2 wt.% if other information is not given.

[$]We make the simplifying assumption that $a_i = R_i$ for this scaling analysis.

604

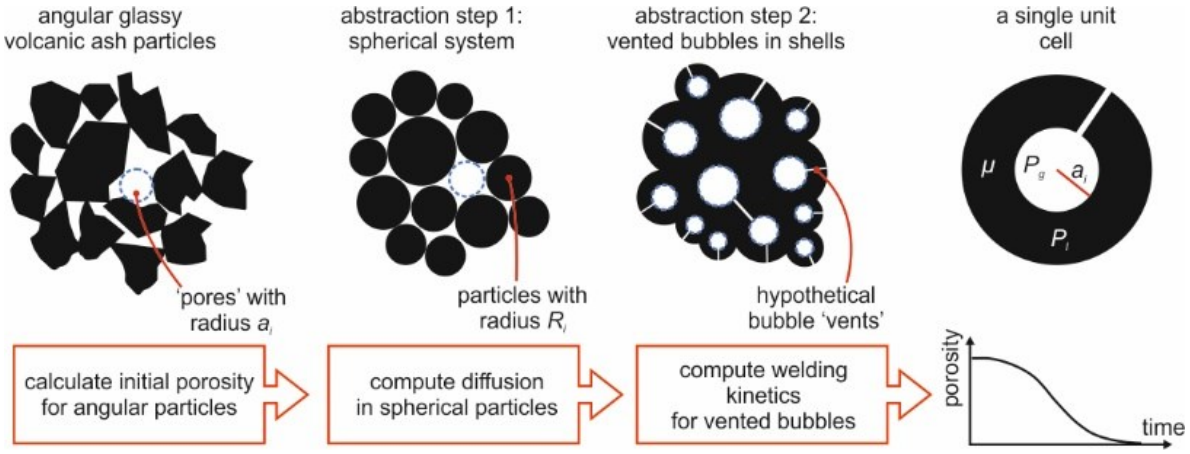

605

606 **Figure 1.** The development of a diffusion–welding model. The natural system is composed of
607 angular volcanic particles, which are abstracted to a pack of spherical particles with the same
608 initial porosity. The diffusion model is used (Eq. 3) to compute the average water content as a
609 function of time $\langle C \rangle (R_i, t)$, which is converted to an average viscosity $\langle \mu \rangle$. Then we make a
610 further abstraction to vented bubble geometry and the welding is computed in terms of an
611 evolution of the total porosity with time $\phi(t)$ using Eqs 1-2, accounting for the polydispersivity
612 of the initial particle size distribution (Wadsworth et al. 2017b).

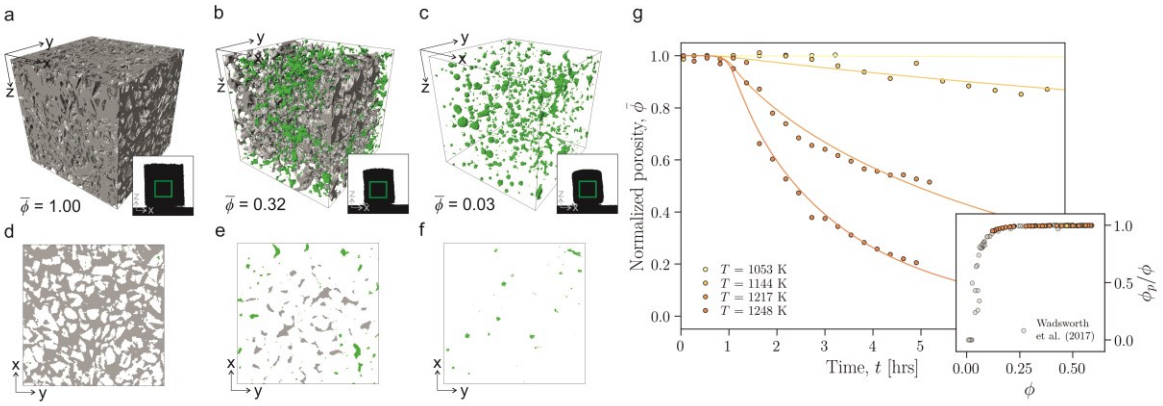

[Full page width]

Figure 2. Constraints of time-dependent welding collected *in situ* using either optical dilatometry or x-ray tomography. **a-c**, 3-dimensional rendered images of the time-dependent welding process segmented on the basis of grayscale gradient filtering from continuous, time-resolved, *in situ* x-ray tomography data. The particle phase is rendered transparent, and the pore phase is divided into a grey and a green component depending on whether it is connected across the sample in any direction (grey) or is isolated from connections (green). Box edge lengths of the sub-volume displayed are 350 µm. Displayed is one representative experiment performed at $T = 1350$ K, for which the dimensionless porosity $\bar{\phi}$ is labelled. Inset in each panel is the 2-dimensional side-view of an initially cylindrical sample from an experiment at the same conditions performed in the optical dilatometer (image base length of 5 mm). **d-f**, a 2-dimensional horizontal slice through each of the 3-dimensional rendered images in **a-c** taken at the midpoint of the z-axis in the sample. **g**, The porosity as a function of time of the obsidian particles sintered *in situ* using time-resolved x-ray tomography at a range of temperatures (labelled). The curves represent the solutions to Eqs 1 or 2 with $\bar{P} = 0$ and computing the time-dependent diffusion of volatiles out of the particles (Eq. 4). *Inset:* the connectivity of the pore phase with porosity showing the collapse from fully connected to isolated as $\phi \rightarrow \phi_c$

during welding. Data are compared with welding in synthetic glass systems (Wadsworth et al. 2017a).

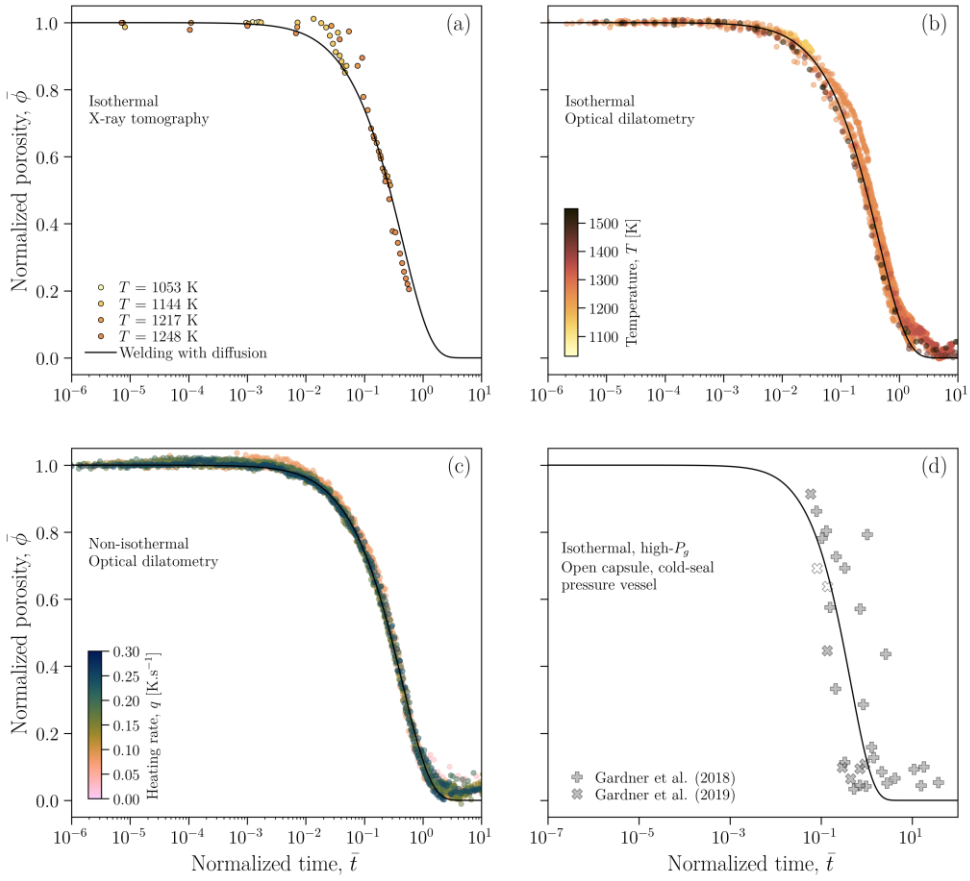

[full page width]

Figure 3. Modeling the evolution of the pore phase between the welding droplets. **a**, the porosity $\bar{\phi}$ as a function of time for each experimental T for the x-ray tomography experiments only. These data are compared with the results of Eq. 2 (welding) with Eq. 4 (diffusion), which account for syn-welding degassing of the droplets and which require no fitting parameters. These data are the same as those presented in Figure 2g. **b**, the same as **a** but for the data collected using optical dilatometry (i.e. without 3-dimensioanl microstructural information) showing that this technique can be used to capture the bulk decay of porosity with time. **c**, the same dimensionless plot as in **b** but for non-isothermal experiments at different experimental heating rates, showing that regardless of the $T(t)$ path taken by the samples, the efficacy of our model (Eqs 4-6) is robust. In all panels, the dimensionless time is given by Eq. 3. **d**, The data from Gardner et al. (2018) and Gardner et al. (2019) collected using a high-P_g cold seal vessel, re-analysed using the diffusion-welding model given here. The filled points represent data for

650 which rhyolite particles are hydrating (from $C_i = 0.15$ wt.% to equilibrium conditions at high
651 P_g and high T) while welding, and the un-filled points represent data for which rhyolite particles
652 are de-hydrating (from $C_i = 2.3$ wt.% to equilibrium conditions at high P_g and high T). See the
653 papers originating the data for more information.
654

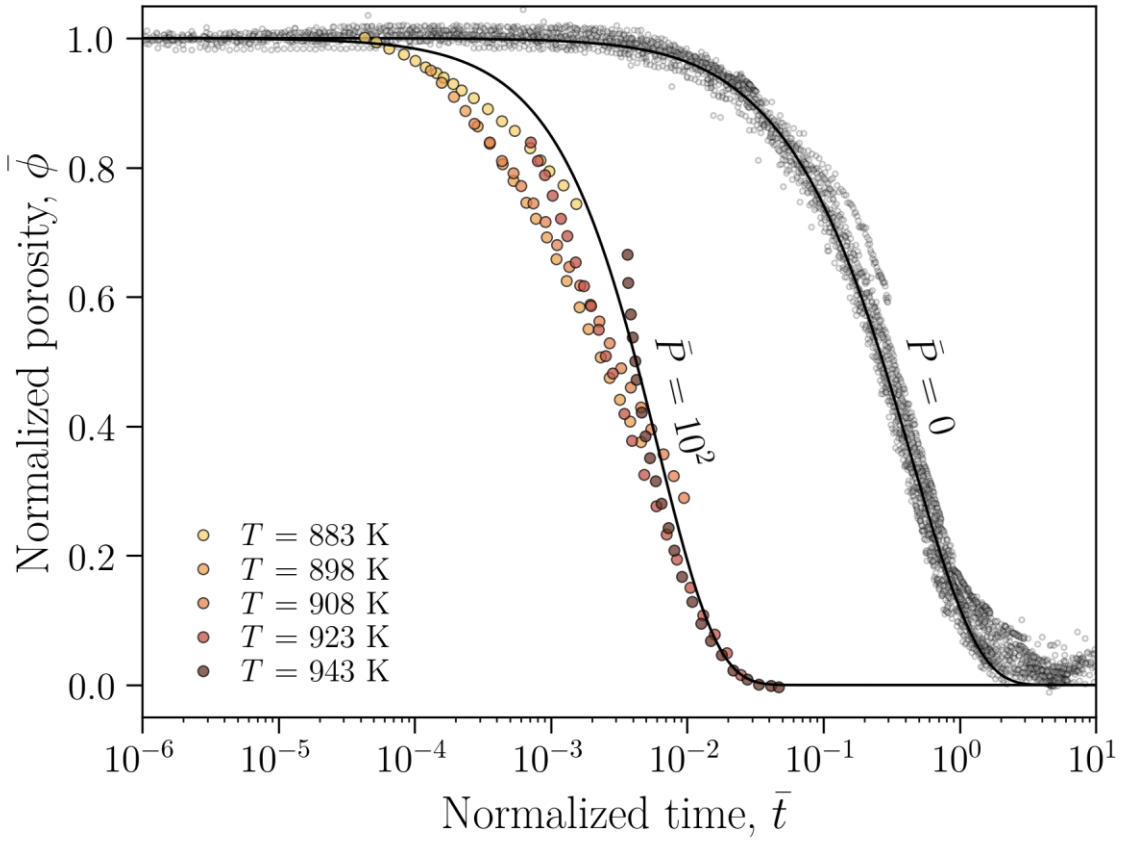

[half-page width or less]

Figure 4. The effect of pressure on the welding of glassy particles. Shown here are data from *Friedman et al.*, [1963], in which synthetic glass particles (Pyrex™) are welded under a pressure equivalent to $\bar{P} = 100$, and at a range of temperatures (labelled). We use the values of μ, R_i and P_l given in their work, and the curve represents the solution to Eq. 2 without fitting parameters. Shown for reference is the solution for $\bar{P} = 0$ and all data from Figure 3 given in grey. In all cases, the dimensionless time is given by Eq. 3.

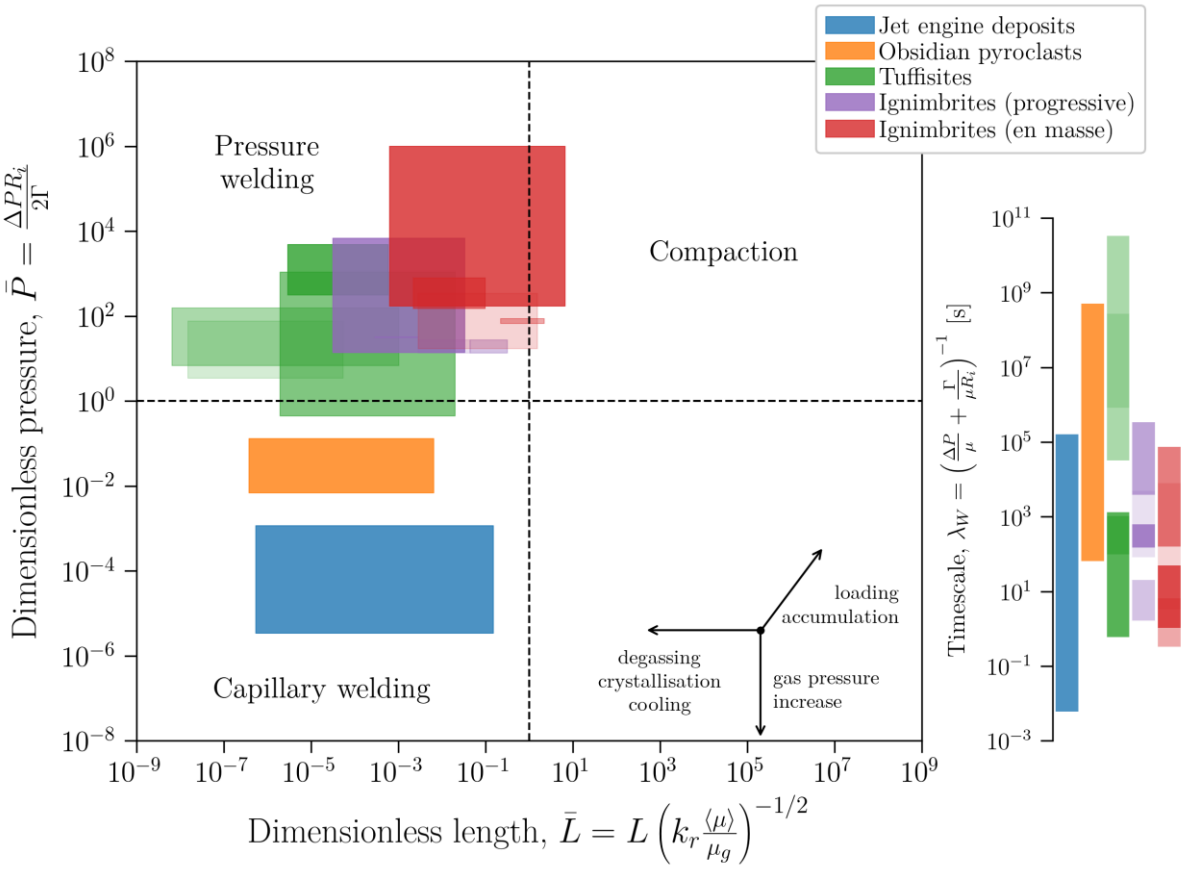

[1/2 page width or less]

Figure 5. Scenarios and regimes for volcanic welding. A plot of $\bar{P}$ and $\bar{L}$ regimes for volcanic welding with the range of conditions for natural examples given using constraints compiled in Table 1.